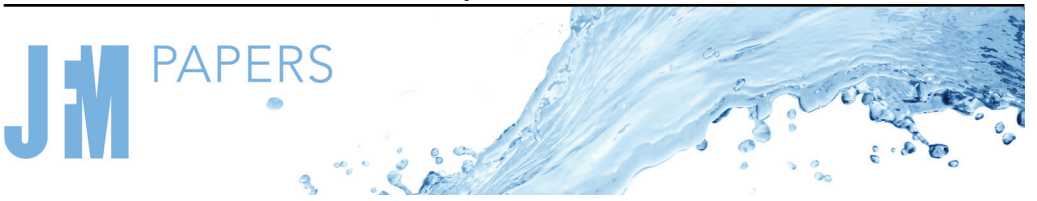
J. Fluid Mech. (2026), *vol.* 1026, A11, doi:10.1017/jfm.2025.11006



Marangoni-driven freezing dynamics of supercooled binary droplets

Feng Wang[1], **Hao Zeng**[1], **Yihong Du**[1], **Xinyu Tang**[1] **and Chao Sun**[1,2]

[1]New Cornerstone Science Laboratory, Center for Combustion Energy, Key Laboratory for Thermal Science and Power Engineering of Ministry of Education, Department of Energy and Power Engineering, Tsinghua University, Beijing 100084, PR China

[2]Department of Engineering Mechanics, School of Aerospace Engineering, Tsinghua University, Beijing 100084, PR China

Corresponding author: Chao Sun, chaosun@tsinghua.edu.cn

(Received 3 February 2025; revised 11 November 2025; accepted 12 November 2025)

Solidification of droplets is of great importance to various technological applications, drawing considerable attention from scientists aiming to unravel the fundamental physical mechanisms. In the case of multicomponent droplets undergoing solidification, the emergence of concentration gradients may trigger significant interfacial flows that dominate the freezing dynamics. Here, we experimentally investigate the fascinating interfacial freezing dynamics of supercooled ethanol–water droplets, accompanied with the migration and growth of massive ice particles. We reveal that this unique freezing dynamics is driven by solidification-induced solutal Marangoni flow within the droplets. Our model, which incorporates the temperature- and concentration-dependent properties of the ethanol–water mixture, quantitatively predicts both the migration velocity and the growth rate of the ice particles. The former is determined by the solutal Marangoni flow velocity, while the latter is governed by a balance between the latent heat release and the enhanced thermal dissipation by the Marangoni flow. Moreover, we show that the final wrapping state of droplets can be modulated by the concentration of ethanol. Our findings may pave the way for novel insights into the physicochemical hydrodynamics of multicomponent liquids undergoing phase transitions.

Key words: drops, solidification/melting

1. Introduction

Solidification of droplets is ubiquitous in both natural environments and industrial applications. The accumulation of frozen droplets on artificial surfaces can lead to a

© The Author(s), 2025. Published by Cambridge University Press.

https://doi.org/10.1017/jfm.2025.11006 Published online by Cambridge University Press

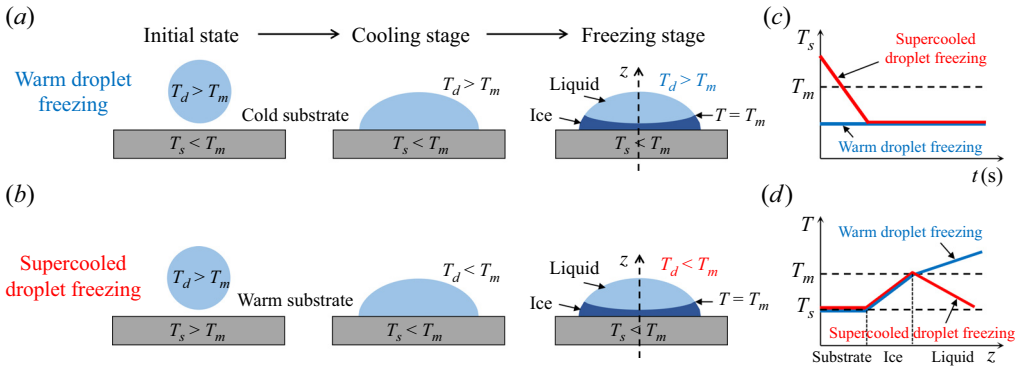


Figure 1. Schematic diagrams illustrating droplet freezing dynamics. (*a*) For warm droplets, the liquid phase temperature T_d remains above the freezing point T_m, so the released latent heat at the freezing front is primarily dissipated via ice-phase conduction. (*b*) In contrast, supercooled droplets (with $T_d < T_m$) enable additional heat dissipation through the supercooled liquid during freezing. (*c*) Substrate temperature profiles over time comparing warm (blue) and supercooled (red) droplet freezing scenarios. (*d*) Temperature profiles along the dashed line in (*a*,*b*) during solidification for warm (blue) and supercooled (red) droplet freezing, showing distinct thermal behaviours.

range of detrimental consequences to aviation safety (Cebeci & Kafyeke 2003), maritime operations (Dehghani-Sanij *et al.* 2017) and wind turbines (Makkonen *et al.* 2001) in the cold regions. Substantial efforts have been dedicated to enhancing our understanding of the intricate dynamics of freezing droplets (Zadražil *et al.* 2006; Tembely & Dolatabadi 2019; Kant *et al.* 2020*a*; Koldeweij *et al.* 2021; Grivet *et al.* 2022; Kavuri *et al.* 2023, 2025) covering a wide array of factors, such as the influence of environmental medium (Graeber *et al.* 2017; Lambley *et al.* 2023; Lyu *et al.* 2023), the inertia of droplets (Hu *et al.* 2020; Thiévenaz *et al.* 2019, 2020), the composition of droplets (Kharal & Louf 2023; Zeng *et al.* 2023; Jiang *et al.* 2024) and the characteristics of substrates (de Ruiter, Soto & Varanasi 2018; Lolla *et al.* 2022; Wang *et al.* 2023).

Based on the temperature of the remaining liquid during solidification, droplet freezing systems can be categorised into two types: (i) warm droplet freezing (figure 1*a*) and (ii) supercooled droplet freezing (figure 1*b*). In the case of warm droplet freezing, the initial droplet temperature T_d is higher than the freezing point T_m, while the initial substrate temperature T_s is lower than the freezing point T_m, as illustrated by the blue solid line in figure 1(*c*). Owing to the presence of potential ice nucleation sites on the undercooled substrate, such as pre-existing frost droplets and ice layers (Lolla *et al.* 2022; Zeng, Wang & Sun 2024), the droplet starts to solidify immediately upon contact with the undercooled substrate. During this process, the temperature of the remaining liquid stays above the freezing point (Wang *et al.* 2024), as demonstrated by the blue solid line in figure 1(*d*). Consequently, the latent heat released at the ice front can only be consumed through heat conduction via the ice phase. In contrast, when it comes to the freezing of supercooled droplets, at the initial state, both the droplet temperature T_d and the substrate temperature T_s are higher than the freezing point T_m. Subsequently, the substrate is gradually cooled to a temperature below the freezing point, as indicated by the red solid line in figure 1(*c*). Simultaneously, the droplet is also cooled and enters a supercooled state (Schremb *et al.* 2017; Chu *et al.* 2024) due to the ice nucleation energy barrier. Then, the supercooled droplet undergoes a transition from its supercooled state to a mixture of ice and liquid water at the freezing temperature, which is referred to as the recalescence stage (Sebilleau *et al.* 2021). The red solid line in figure 1(*d*) represents the typical temperature

https://doi.org/10.1017/jfm.2025.11006 Published online by Cambridge University Press

distribution along the centreline of the freezing supercooled droplet, as marked by the dashed line in figure 1(*b*). Throughout solidification, the temperature of the remaining liquid remains supercooled (Schremb *et al.* 2017). As a result, the latent heat released at the ice front can be consumed not only by heat conduction through the ice phase but also by heat transfer within the supercooled liquid.

The freezing dynamics varies significantly between supercooled droplets and warm droplets on cold surfaces. For warm pure water droplets, a unidirectional ice front advancing away from the cold substrate was observed (Marin *et al.* 2014). This is attributed to the dominant heat conduction through the ice phase, which dissipates the latent heat released during solidification. Conversely, during the solidification of supercooled water droplets on a cold wall, dendritic freezing dynamics were identified (Schremb *et al.* 2017). This process requires consideration of heat conduction in both the supercooled liquid and the adjacent solid substrate. Similarly, the freezing dynamics of warm saline droplets resembles those of warm pure water droplets, with a slight difference in the tip angle formed at the top of the droplets (Boulogne & Salonen 2020). This difference arises from the volume expansion during solidification (Marin *et al.* 2014). However, for supercooled saline droplets, an unexpected interfacial ice sprouting dynamics has been reported (Chu *et al.* 2024). This unique phenomenon is attributed to the formation of a brine film during the nucleation and recalescence process, which is accompanied by salt rejection.

To further explore the impact of composition changes on freezing dynamics, the role of the solutal Marangoni effect becomes particularly interesting. If the composition rejected near the ice front can significantly alter surface tension, a strong solutal Marangoni effect may arise within the droplets, potentially influencing their freezing dynamics. Wang *et al.* (2024) observed this effect in warm ethanol–water droplets on a cold substrate, reporting the self-lifting freezing dynamics. The solutal Marangoni flow, driven by ethanol enrichment at the ice front, created a pronounced dynamic growth angle at the liquid–solid–gas tri-junction, resulting in the nearly doubling of the droplets' final height due to geometrical effects (Anderson, Worster & Davis 1996).

Building on these understandings, we now turn to the question of what occurs during the solidification of supercooled ethanol–water droplets on a cold surface. The nucleation and growth of ice crystals accompanied with the rejection of ethanol may involve more intricate physical phenomena than those in previous work. The presence of Marangoni flow could significantly enhance convective heat transfer and mass transport, leading to novel freezing dynamics in supercooled ethanol–water droplets.

Here, we investigate experimentally the fascinating migration and growth dynamics of ice particles at the interface of supercooled ethanol–water droplets. This phenomenon is propelled by solutal Marangoni flow (Wang *et al.* 2024), which arises from the localised enrichment of ethanol near the ice front (Dedovets, Monteux & Deville 2018). Our findings reveal that this unique freezing dynamics is driven by solidification-induced solutal Marangoni flow. Using a model that accounts for the property variations of the ethanol–water mixture, we achieve quantitative agreement with experiments on two key aspects: the ice particle migration velocity, predicted by the solutal Marangoni flow speed, and its growth rate, modelled by balancing latent heat release against solutal-Marangoni-enhanced thermal dissipation. This novel interfacial freezing process culminates in the formation of beautiful patterns covered by ice particles (Ahmadi *et al.* 2019), the distinctive dimensions of which are found to depend on the concentration of ethanol.

The paper is organised as follows. Section 2 describes the experimental set-up and the properties of the binary droplets. Section 3 describes the experimental results, providing a general picture of the interfacial freezing dynamics of supercooled binary droplets. In § 4, we focus on the interfacial temperature evolution of the supercooled binary droplets.

https://doi.org/10.1017/jfm.2025.11006 Published online by Cambridge University Press

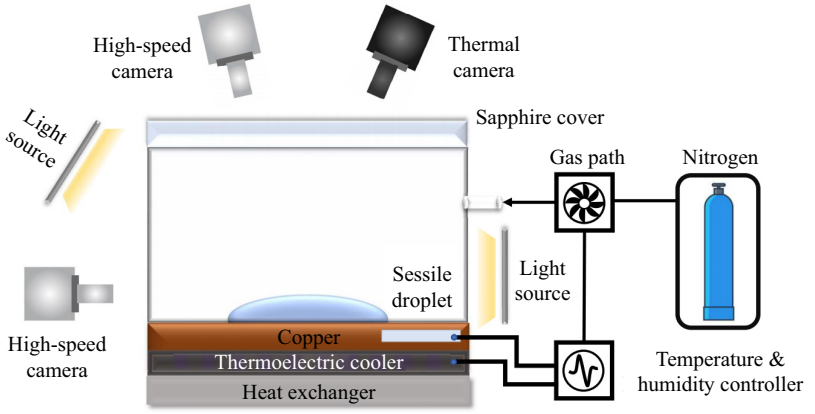


Figure 2. Schematic view of the experimental set-up. In the experiments, the droplet is gently deposited onto the copper substrate, with both the droplet and substrate preconditioned to room temperature. Subsequently, the substrate undergoes progressive cooling down to $T_s = -20\,^{\circ}\mathrm{C}$ by a semiconductor cooler.

In § 5, we elucidate the Marangoni-driven dynamics of the ice particles at the droplet–air interface. Finally, we end with conclusions and discussions in § 6.

2. Materials and methods

Experiments are conducted in a custom-built transparent environmental chamber with internal dimensions of 8 cm × 8 cm × 8 cm. This chamber allows for humidity control and temperature monitoring, as depicted in figure 2. The droplets used in the experiments are either deionised water or ethanol–water solutions. The ethanol, supplied by Shanghai Titan Scientific Co. Ltd (General-reagent, $\geqslant$99.7 %), is mixed with deionised water (18.2 MΩ cm electrical conductivity) from a Milli-Q water purification system (Merck, Germany). Microlitre droplets are generated using a microsyringe and dispensing needle. The substrate is gradually cooled by an embedded semiconductor cooler. A heat exchanger connected to a cold reservoir is attached to the opposite side of the semiconductor to maintain energy balance. A thermocouple, embedded 0.5 mm below the substrate's upper surface, measures its temperature. Connected to a Proportional-Integral-Derivative controller, the thermocouple regulates the power supply to the semiconductor cooler, ensuring a variation of less than 0.2 K during experiments.

In the experiments, droplets with various volume (V_0) and volume fraction of ethanol (c_0) are gently deposited onto the nickel-plated copper substrate at room temperature ($T_0 = 25\,^{\circ}\mathrm{C}$). Then, the substrate is slowly cooled by an embedded peltier cooler down to $T_s = -20\,^{\circ}\mathrm{C}$, and the droplet is gradually cooled into a supercooled state before the sudden nucleation of ice crystals (Chu *et al.* 2024). The freezing dynamics of the droplets is recorded by high-speed cameras (Photron Nova S12) from both the top-down view and side view, and the temperature evolution is recorded by an infrared camera (Telops FAST L200, Stirling-cooled Mercury Cadmium Telluride detector) from the top-down view.

The physical properties of the binary droplets employed in this work are summarised in table 1. The freezing point of the ethanol–water mixture, along with its surface tension and density at $T = 20\,^{\circ}\mathrm{C}$ were determined by fitting polynomial functions to experimental data (Dean 1999; Khattab *et al.* 2012; Kuchuk, Yu & Golikova 2012). The viscosity of the ethanol–water mixture at $T = -20\,^{\circ}\mathrm{C}$ was obtained by interpolating the measurement data from the literature (Halfpap & Sorensen 1982).

https://doi.org/10.1017/jfm.2025.11006 Published online by Cambridge University Press

Concentration c_0 (v/v)	Freezing point T_m (°C)	Surface tension γ (mN m^{-1})	Density ρ (g cm^{-3})	Viscosity μ (mPa s)
0	0	72.41	1.00	4.29
0.05	−1.61	60.30	0.991	5.77
0.10	−3.35	51.49	0.985	8.44
0.15	−5.38	45.14	0.979	11.27
0.20	−7.79	40.79	0.974	14.40
0.37	−20	34.20	0.953	25.67

Table 1. Properties of ethanol–water droplets: surface tension and density at $T = 20\,^{\circ}\mathrm{C}$ and viscosity at $T = -20\,^{\circ}\mathrm{C}$.

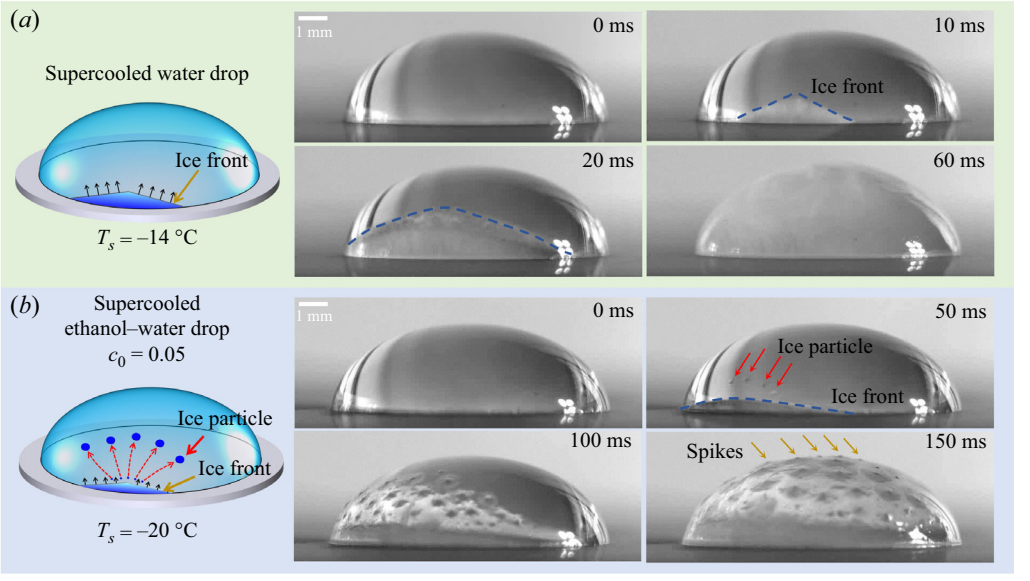


Figure 3. Side view for the freezing dynamics of supercooled droplets. (*a*) In the case of pure water droplets ($V_0 = 150\,\mu$l), the explosive nucleation phenomena (recalescence) is observed, when the substrate temperature T_s is cooled down to approximately $-14\,^{\circ}\mathrm{C}$. (*b*) By contrast, the ethanol–water droplets ($c_0 = 0.05$, $V_0 = 150\,\mu$l) can remain unfrozen for several minutes, with the substrate temperature maintaining $T_s = -20\,^{\circ}\mathrm{C}$. Subsequently, dispersed ice particles are observed at the droplet–air interface, migrating uni-directionally and growing slowly, which is quite different from that of the pure water case.

3. Observation of the interfacial freezing dynamics

Figure 3 presents the typical freezing dynamics of supercooled droplets (see supplementary movie S1 available at https://doi.org/10.1017/jfm.2025.11006). For a pure water droplet ($V_0 = 150\,\mu$l, figure 3*a*), the rapid recalescence process is observed when the substrate temperature approaches the nucleation temperature $T_s \approx -14\,^{\circ}\mathrm{C}$. The dendritic ice front, as indicated by the blue dashed line in figure 3(*a*), advances rapidly with a velocity of approximately 10 cm s^{-1}, aligning with prior studies (Schremb *et al.* 2017). In contrast, for an ethanol–water droplet ($V_0 = 150\,\mu$l, $c_0 = 0.05$, figure 3*b*), the initial formation of the dendritic ice front is also observed, as indicated by the blue dashed line

https://doi.org/10.1017/jfm.2025.11006 Published online by Cambridge University Press

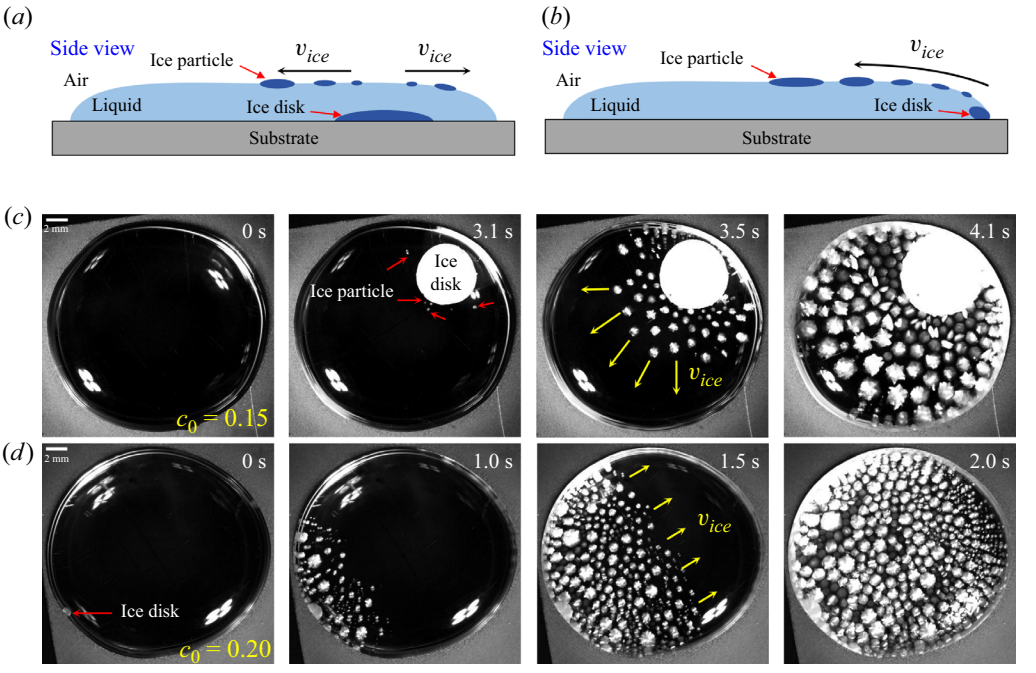


Figure 4. Top-down view for the freezing dynamics of supercooled ethanol–water droplets. (*a*,*b*) Sketch for two typical freezing processes observed in experiments, corresponding to the experimental snapshots (*c*,*d*). Since the ice nucleation process is stochastic, it can occur at the solid–liquid interface (*a*) and near the solid–liquid–air triple point (*b*). (*c*) When the ice nucleation occurs at the solid–liquid interface ($c_0 = 0.15$, $V_0 = 500\ \mu$l, $T_s = -20\ ^\circ$C), an expanding ice disk can be observed from the top-down view. Subsequently, the migrating ice particles are observed, moving away from the centre of the ice disk with a velocity v_{ice}. (*d*) When the ice nucleation occurs near the solid–liquid–air triple point ($c_0 = 0.20$, $V_0 = 500\ \mu$l, $T_s = -20\ ^\circ$C), the ice disk becomes much smaller than that of the former case. Subsequently, the migrating ice particles are observed, moving towards the other side of the droplet.

in figure 3(*b*). However, a surprising phenomenon occurs: ice particles detach and move away from the ice front at the droplet–air interface (indicated by red arrows), migrating toward the droplet's opposite side (as shown by the red dashed line in the schematic of figure 3*b*). These ice particles travel faster than the advancing ice front, with their amount and size progressively increasing, forming spikes at the droplet–air interface (as indicated by the red arrows at $t = 150$ ms).

The observed interfacial freezing dynamics of the supercooled ethanol–water droplet is quite different from that of the recalescent freezing dynamics of the supercooled water droplet. Given the stochastic nature of the initial ice nucleation process (Gurganus, Kostinski & Shaw 2013), we capture the freezing dynamics of the large supercooled binary droplet via a top-down view, as shown in figure 4 and supplementary movie S2. In order to eliminate the curvature effect of the droplet–air interface on the interfacial freezing dynamics, we perform experiments with large droplets ($V_0 = 500\ \mu$l), whose initial deposition diameter ($D_0 \approx 2$ cm) is much larger than the capillary length ($l_c = \sqrt{\gamma/(\rho g)} \approx 2.7$ mm, g is the gravitational constant). As a result, gravity flattens the large droplet into a liquid puddle, which has a large aspect ratio of $D_0/h_0 \approx 10$, where $h_0 = 4V_0/(\pi D_0^2) \approx 1.6$ mm is the average droplet thickness.

In experiments, according to the initial ice nucleation position, the freezing processes of the supercooled ethanol–water droplet can be categorised into two types: (i) ice

https://doi.org/10.1017/jfm.2025.11006 Published online by Cambridge University Press

nucleation occurs at the solid–liquid interface, as sketched in figure 4(*a*); (ii) ice nucleation occurs near the solid–liquid–air triple point, as sketched in figure 4(*b*). When the initial ice nucleation position is far from the liquid–air interface ($V_0 = 500\ \mu$l, $c_0 = 0.15$), the growth of the circular ice disk at the bottom interface of the droplet is observed, as shown in figure 4(*c*), which is similar to previous studies on the ice crystal growing on a undercooled substrate (Grivet *et al.* 2022). Subsequently, some ice particles form at the droplet–air interface within the affected region of the ice disk, as indicated by the red arrows in figure 4(*c*). Then, the ice particles migrate and grow at the droplet–air interface, moving away from the centre of the ice disk, as indicated by the yellow arrows in figure 4(*c*). Finally, the ice particles fully cover the droplet–air interface. When the initial ice nucleation position is near the liquid–air interface or at the liquid–air interface ($V_0 = 500\ \mu$l, $c_0 = 0.20$), the ice disk at the solid–liquid interface is much smaller than that in the former case, as shown in figure 4(*d*). Similarly, massive ice particles are observed forming, migrating and growing at the droplet–air interface, moving uni-directionally towards the other side of the droplet, and ultimately covering the entire interface of the supercooled ethanol–water droplet. Varying the initial ethanol concentration c_0 (e.g. 0.05, 0.10) yields a similar overall process of ice particle migration and growth at the droplet surface, but with a concentration-dependent velocity to be investigated in the following sections.

4. Interfacial temperature evolution of the supercooled binary droplets

To understand the mechanism of the interfacial freezing dynamics, we first use the thermal camera. We investigate the interfacial temperature evolution of the supercooled ethanol–water droplets from the top-down view, as shown in figure 5. The initial temperature of droplets (T_{liq}) approximately equals the substrate temperature T_s, $T_{liq} \approx T_s = -20°$C, which is far below the freezing point (T_m), confirming the supercooled state of droplets. When the initial ice nucleation position is far from the liquid–air interface ($V_0 = 500\ \mu$l, $c_0 = 0.15$), the growth of the circular ice disk at the bottom interface can also be inferred as well from the thermal imaging snapshot, as indicated by the circular warm region within the droplet in figure 5(*a*) ($t = 0.2$ s). Subsequently, when ice particles migrate at the droplet–air interface, due to the released latent heat during the growth of the ice particles, the local temperature near the ice particles increases rapidly to the freezing point ($T_{ice} = T_m$), as shown in figure 5(*a*) ($t = 0.8$ s). Finally, when the ice particles fully cover the droplet–air interface, the interfacial temperature of the droplet approximately equals the freezing point T_m. When the initial ice nucleation position is near the liquid–air interface or at the liquid–air interface ($V_0 = 500\ \mu$l, $c_0 = 0.20$), the interfacial temperature evolution is similar to that in the former case.

To obtain the typical velocity of the interfacial freezing dynamics from the thermal imaging snapshots, we extract the temperature distribution along the centreline of the droplet (figure 5*c*,*d*), indicated by the white dashed line in figure 5(*a*,*b*). Analysing the transition points of the temperature profiles, indicated by the red circles in figure 5(*c*,*d*), yields the typical migrating velocity of ice particles v_{ice}. Furthermore, the temperature profiles in figure 5(*c*,*d*) are replotted into spatiotemporal phase diagrams, as shown in figure 6(*a*,*b*). The horizontal axis represents time, and the vertical axis represents space. The slope in the spatiotemporal diagrams, indicated by the white dashed line, determines the typical migrating velocity of ice particles v_{ice}. For the given substrate temperature $T_s = -20\ °$C, the migrating velocity of ice particles v_{ice} is found to decrease with the ethanol concentration c_0.

https://doi.org/10.1017/jfm.2025.11006 Published online by Cambridge University Press

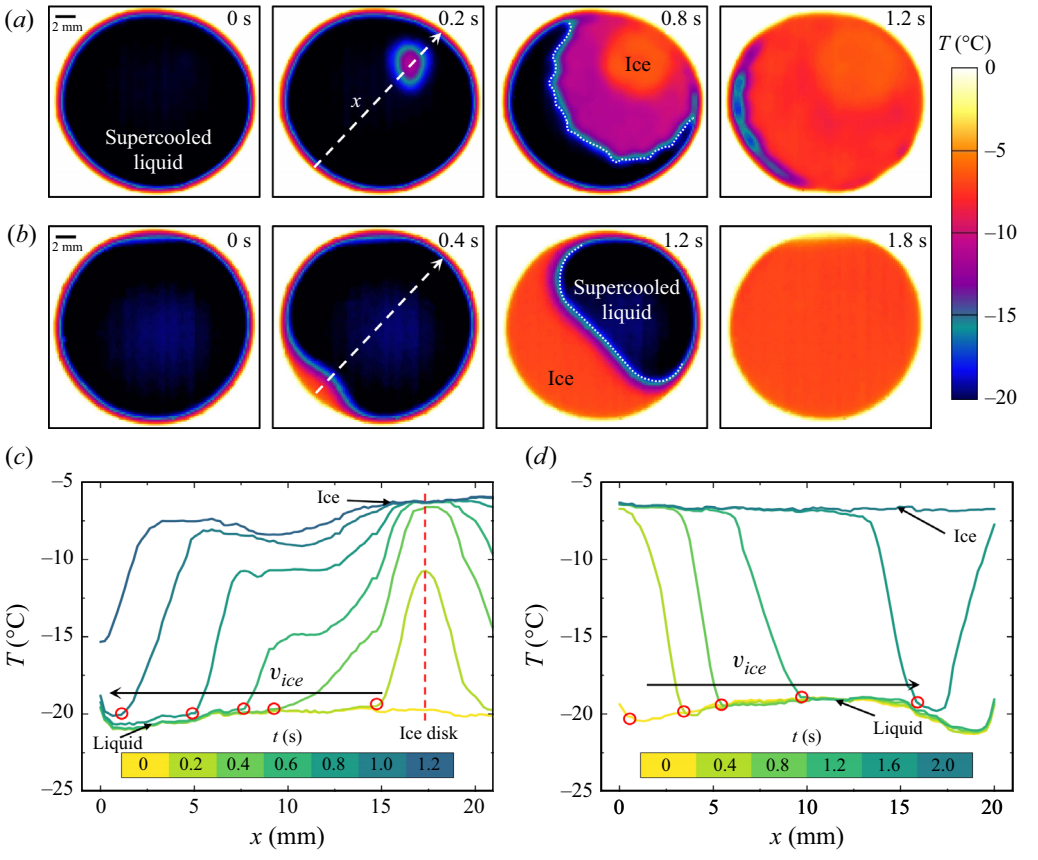


Figure 5. Thermal imaging for the freezing supercooled ethanol–water droplets. (*a*) Top-down view for the case of ice nucleates at the solid–liquid interface ($c_0 = 0.15$, $V_0 = 500\,\mu$l, $T_s = -20\,^\circ$C). (*b*) Top-down view for the case of ice nucleates near the solid–liquid–air triple point ($c_0 = 0.20$, $V_0 = 500\,\mu$l, $T_s = -20\,^\circ$C). (*c*,*d*) Temperature distribution along the white dashed line (horizontal axis x) in (*a*,*b*), respectively. The temperature of the supercooled liquid T_d is almost equal to the substrate temperature $T_s = -20\,^\circ$C. The white dotted lines in (*a*,*b*) and the red circles in (*c*,*d*) are for the ice–water interface.

5. Marangoni-driven dynamics of ice particles

In order to fully understand the concentration-related mechanism of the interfacial freezing dynamics, we track the migration and growth of individual ice particles using the open-source software, ImageJ (Schneider, Rasband & Eliceiri 2012), as sketched in figure 7(*a*) (details for image-processing procedure can be found in Appendix A). The displacement of ice particles ξ as a function of time, at different ethanol concentrations c_0, is depicted in figure 7(*b*). From this plot, it is found that the displacement of ice particles ξ increases almost linearly with time. In other words, the ice particles migrate at the droplet–air interface with a constant velocity v_{ice}. By fitting the experimental results with the linear functions indicated by the red solid line in figure 7(*b*), the migrating velocity of the ice particles v_{ice} can be determined from the slope. Furthermore, it is found that the migrating velocity v_{ice} decreases with the ethanol concentration c_0, which is consistent with the results obtained from the thermal imaging snapshots in figure 6. Similarly, as shown in figure 7(*c*), the radius of the ice particles R_{ice} is also found to increase almost linearly with time. By fitting the experimental results with the linear functions indicated by the red solid line in figure 7(*c*), the growth rate of the ice particles $\dot{R}_{ice}$ can be determined

https://doi.org/10.1017/jfm.2025.11006 Published online by Cambridge University Press

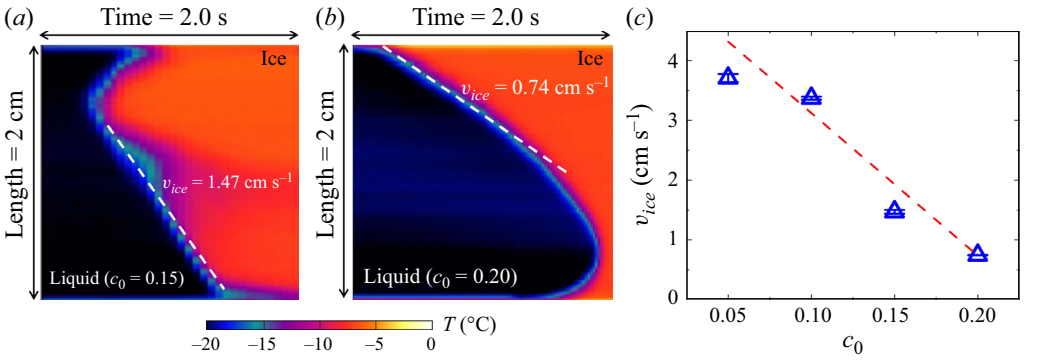


Figure 6. Spatiotemporal diagrams of thermal imaging snapshots. (*a*,*b*) Spatiotemporal diagrams corresponding to the thermal snapshots in figure 5(*a*,*b*), respectively. From the spatiotemporal diagrams, the typical migrating velocity of ice particles v_{ice} can be determined, as indicated by the white dashed line. (*c*) The migrating velocity of ice particles v_{ice} at different ethanol concentrations c_0. The blue triangles represent the experimental data, and the red dashed line represents the linear fitting result. For the given substrate temperature $T_s = -20$ °C, the migrating velocity of ice particles v_{ice} decreases with the ethanol concentration c_0. The error bars in (*c*) are for the standard deviations obtained from the linear fits.

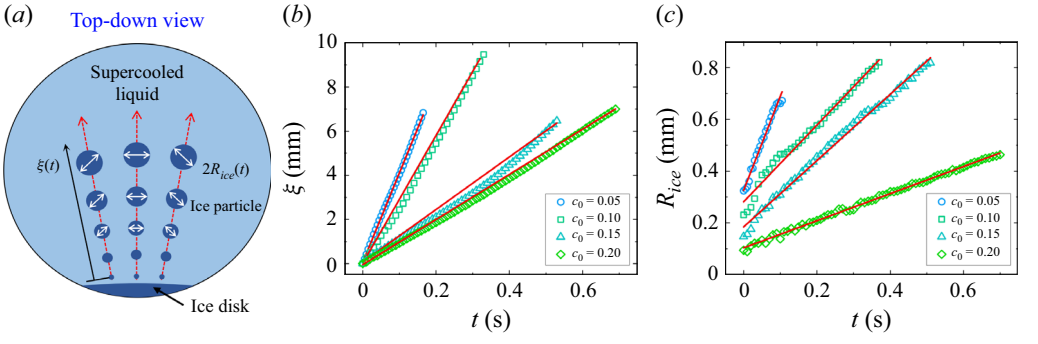


Figure 7. Dynamics of migration and growth of the dispersed ice particles at the droplet–air interface. (*a*) Top-down view sketch for the migration and growth of the dispersed ice particles at the droplet–air interface. (*b*) The displacement of ice particles ξ and (*c*) the equivalent radius of ice particles R_{ice} as a function of time, at different ethanol concentrations c_0. The dots are for the experimental data, and the red solid lines are for the linear fitting results.

from the slope, and it is also found that the growth rate $\dot{R}_{ice}$ decreases with the ethanol concentration c_0.

5.1. *Marangoni-driven migration of ice particles*

Considering the small Stokes number of the migrating ice particles $Stk = \rho v_{ice} R_{ice}/(18\mu) < 0.1$, we assume that the migration velocity of the ice particles v_{ice} is determined by the solutal Marangoni flow at the droplet–air interface, as sketched in figure 8(*a*). During solidification of supercooled ethanol–water droplets, the local concentration of ethanol c_{high} in the vicinity of the ice front increases, reaching the saturation concentration c_{sat}, at which $T_m(c_{sat}) = T_s$. Consequently, the surface tension γ_{low} near the ice front is smaller than that away from the ice front γ_{high}, which triggers the solutal Marangoni flow across the droplet and drives ice particles to move (Lohse & Zhang 2020). Then, the migration velocity v_{ice} can be estimated by balancing the Marangoni stress $\Delta\gamma/D_0$ with the viscous stress $\mu v_m/l$,

https://doi.org/10.1017/jfm.2025.11006 Published online by Cambridge University Press

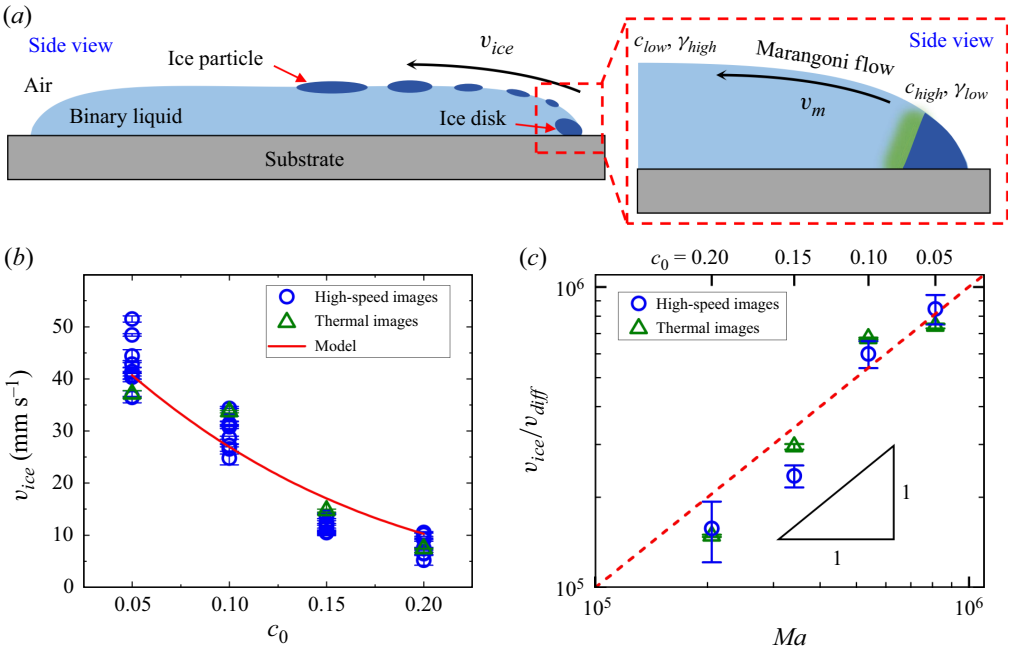


Figure 8. Migrating velocity of the ice particles. (*a*) The side view for the sketch of ice particle migration, and the zoomed-in figure is the side view for the sketch of solutal Marangoni flow near the solid–liquid–air triple point. During the formation of the ice disk, the ethanol is rejected from the ice, leading to the local enrichment of ethanol concentration c_{high} and the decrease of surface tension γ_{low}. While the ethanol concentration far away from the ice-water interface $c_{low} \approx c_0$ remains almost undisturbed, and the local surface tension γ_{high} is higher than γ_{low}. Therefore, the surface tension gradient triggers the solutal Marangoni flow v_m away from the triple point, which drives the motion of ice particles. (*b*) The migrating velocity of ice particles v_{ice} as a function of the ethanol concentration c_0. (*c*) The dimensionless migrating velocity of ice particles v_{ice}/v_{diff} as a function of Marangoni number Ma. The dots are for the experimental data, the red solid line is for the model prediction of v_{ice}, and the red dashed line is for the scaling relation $v_{ice}/v_{diff} \sim Ma$. The error bars in (*b*) are for the standard deviations obtained from the linear fits, and the error bars of blue circles in (*c*) are for the standard deviation calculated from at least 10 data points.

$$v_{ice} = v_m = \frac{\Delta\gamma l}{\mu D_0}, \tag{5.1}$$

where μ is the viscosity of the binary mixture at the saturated concentration $c_{sat} = 0.37$, $D_0 = 2$ cm is the droplet diameter, $l = h_0/2$ is the typical length scale, taken as half the average droplet thickness $h_0 = V_0/(\pi R_0^2) \approx 1.6$ mm to account for the compensating flow near the substrate (Gelderblom, Diddens & Marin 2022). Here, $\Delta\gamma = \gamma_0 - \gamma_{sat}$ is the typical surface tension difference; the surface tension far from the ice front γ_0 remains the initial state, which is determined by the initial concentration c_0, and the surface tension near the ice front γ_{sat} is determined by the saturated state, determined by the saturated concentration c_{sat}, as listed in table 1. It should be noted that the ice formed in a binary liquid system is considered to be porous (Wei, Zhang & Ni 2025), which is similar to sea ice (Du *et al.* 2023, 2025). While the ice phase consists solely of water, the porous ice is filled with the concentrated ethanol–water mixture. Therefore, we assume a saturated concentration near the ice front.

After incorporating the concentration-dependent properties of the ethanol–water mixture, the estimated ice particle migration velocity v_{ice} (5.1) agrees well with the experimental observations, as shown in figure 8(*b*). The minor discrepancies can likely

https://doi.org/10.1017/jfm.2025.11006 Published online by Cambridge University Press

be attributed to several factors: (i) potential contamination by impurities or surfactants, as reported by Marin *et al.* (2016, 2019); Diddens (2017); (ii) the finite thickness of the ice particles, which reduces the liquid film thickness above the substrate and increases viscous dissipation; (iii) the use of liquid properties (surface tension and density) measured at room temperature, while the experiments were conducted under an undercooling of $T = -20\,^{\circ}\mathrm{C}$; (iv) possible collective effects arising from interactions between multiple ice particles; (v) the limited applicability of the model's simplifying assumptions as the ice particles grow larger and migrate away from the source toward the droplet edge.

Qualitatively, for a given substrate temperature, the migration velocity v_{ice} is found to decrease with concentration c_0 as shown in figure 8(*b*), which arises from the concentration-related surface tension difference $\Delta\gamma(c_0)$. Considering $\Delta\gamma(c_0) = \gamma_0(c_0) - \gamma_{sat}$, the initial surface tension γ_0 decreases with concentration c_0, while the saturated surface tension γ_{sat} is almost constant for the given substrate temperature T_s. Thus, both $\Delta\gamma$ and v_{ice} decrease with concentration c_0.

Additionally, it should be noted that, although the temperature gradient in figure 5 might trigger the thermal Marangoni flows to drive the ice particle to move, the thermal Marangoni effect is much weaker than the solutal Marangoni effect in our experiments. The typical surface tension difference induced by temperature $\Delta\gamma_T$ can be estimated by $\Delta\gamma_T \sim |\mathrm{d}\gamma/\mathrm{d}T|\Delta T < 2$ mN/m, where $|\mathrm{d}\gamma/\mathrm{d}T| \approx 2 \times 10^{-4}$ N/(m K), and the temperature difference $\Delta T = T_m - T_s < 20$ K, while the typical surface tension difference induced by the ethanol concentration $\Delta\gamma_c$ should be of the order of 10 mN/m, as listed in table 1. As a result, the thermal Marangoni effect on interfacial freezing dynamics could be ignored in the present work.

Furthermore, the migrating velocity of the ice particles v_{ice} is non-dimensioned by the typical velocity of solute diffusion $v_{diff} = \mathscr{D}/D_0$, where $\mathscr{D} = 1 \times 10^{-9}$ m^2 s^{-1} is the mass diffusivity of ethanol in water and D_0 is the diameter of the droplet. Then, the dimensionless migrating velocity v_{ice}/v_{diff} can be described by the solutal Marangoni number Ma:

$$\frac{v_{ice}}{v_{diff}} = \frac{\Delta\gamma h}{2\mu\mathscr{D}} = Ma. \tag{5.2}$$

This scaling relation (5.2) agrees well with the experimental data, as shown in figure 8(*c*). Indeed, the dimensionless migrating velocity v_{ice}/v_{diff} also reflects the effective Péclet number Pe at the droplet–air interface, $Pe = D_0 v_{ice}/\mathscr{D} = v_{ice}/v_{diff}$. Hence, the large dimensionless migrating velocity $v_{ice}/v_{diff} \gg 1$ in figure 8(*c*) suggests the effective Péclet number $Pe \gg 1$, and convection is dominant at the droplet–air interface.

5.2. *Marangoni-driven growth of ice particles*

Similarly, we turn to analysing the physical mechanism of ice particle growth. As sketched in figure 9(*a*), ice particles migrate uni-directionally with a constant velocity v_{ice} at the droplet–air interface. For the leading ice particles (as sketched in the red dashed box), the interfacial temperature behind the ice particles approximately equals the freezing point T_m, while the interfacial temperature ahead of the ice particles remains supercooled $T_{liq} = T_s < T_m$, as revealed by the thermal snapshots in figure 5. The growth dynamics of ice particles can therefore be modelled with the classical two-phase Stefan problem (Ahmadi *et al.* 2019; Huerre *et al.* 2021), in which the latent heat is gradually dissipated into the heat sink (the supercooled liquid) to keep the system at or just below the freezing point. By balancing the thermal fluxes at the ice–water interface, the growth rate of the ice particles $\dot{R}_{ice}$ can be expressed as follows:

https://doi.org/10.1017/jfm.2025.11006 Published online by Cambridge University Press

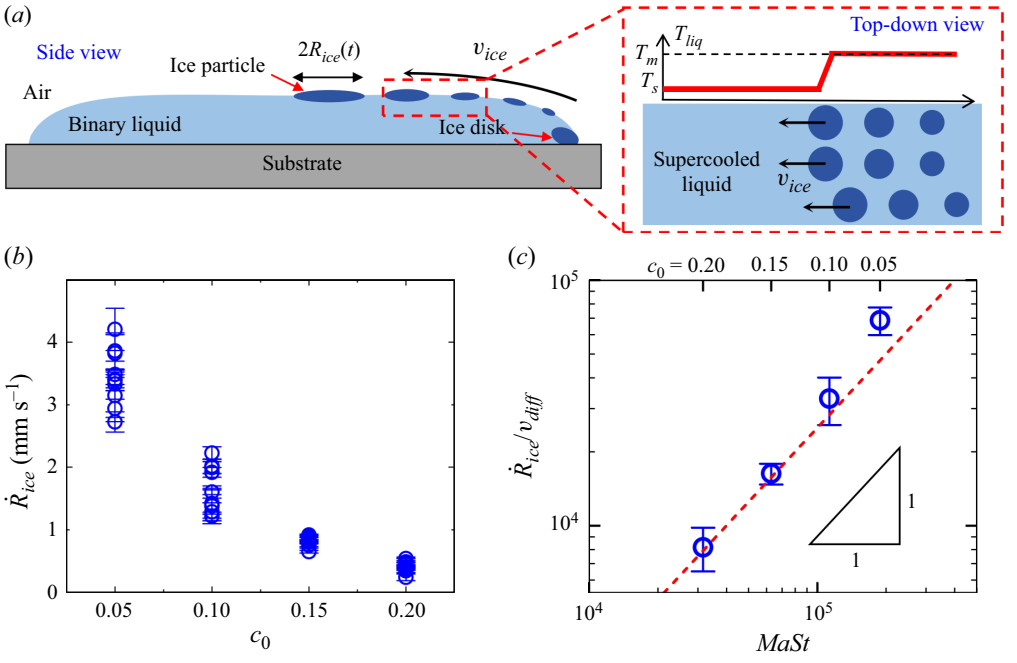


Figure 9. Growth rate of the ice particles. (*a*) The side view for the sketch of ice particle growth, and the zoomed-in figure is the top-down view for the sketch of the temperature distribution around the ice particle. According to the thermal snapshots, the liquid ahead of migrating ice particles remains supercooled. Therefore, the heat transfer within the supercooled liquid predominantly consumes the released latent heat during ice particle growth. (*b*) The growth rate of ice particles $\dot{R}_{ice}$ as a function of the ethanol concentration c_0. (*c*) The dimensionless migrating velocity of ice particles $\dot{R}_{ice}/v_{diff}$ as a function of Marangoni number Ma and Stefan number St. The dots are for the experimental data, the red solid lines are for the model predictions, and the red dashed line is for the scaling relation $\dot{R}_{ice}/v_{diff} \sim MaSt$. The error bars in (*b*) are for the standard deviations obtained from the linear fits, and the error bars in (*c*) are for the standard deviation calculated from at least 10 data points.

$$\rho_l L_f \dot{R}_{ice} = k_i \nabla T_i - k_l \nabla T_l, \tag{5.3}$$

where ρ_l and L_f are the density of liquids and the latent heat of solidification, k_i, k_l are the thermal conductivities of the ice phase and the liquid phase, T_i, T_l are the temperatures within the ice phase and the liquid phase.

Since the ice particles migrate along the droplet–air interface, the released latent heat is dissipated primarily into the supercooled liquid (see the last term in (5.3)). Consequently, we need to account for the convective heat transfer induced by the particle migration velocity v_{ice}. Considering the quasi-static advection–diffusion equation,

$$v_{ice} \nabla T_l = \alpha_l \nabla^2 T_l, \tag{5.4}$$

where $\alpha_l = k_l/(\rho_l c_p)$ is the thermal diffusivity coefficient of the liquid, c_p is the specific heat capacity of liquid.

Assuming a typical length scale l^*, (5.3) simplifies to $\rho_l L_f \dot{R}_{ice} = k_l \Delta T / l^*$, and (5.4) reduces to $v_{ice} \Delta T / l^* = \alpha_l \Delta T / l^{*2}$. Then, by combining (5.3) and (5.4) to eliminate l^*, the growth rate of the ice particles $\dot{R}_{ice}$ can be expressed as follows:

$$\dot{R}_{ice} = \frac{v_{ice} k_l \Delta T}{\alpha_l \rho_l L_f}. \tag{5.5}$$

https://doi.org/10.1017/jfm.2025.11006 Published online by Cambridge University Press

Qualitatively, the growth rate of the ice particles $\dot{R}_{ice}$ is also found to decrease with concentration c_0, as shown in figure 9(*b*). The reason is that for a given substrate temperature T_s, with increasing concentration c_0, the freezing point of the binary droplets T_m decreases, and thus the supercooling temperature decreases $\Delta T(c_0) = T_m(c_0) - T_s$. Thus, both v_{ice} and ΔT decrease with c_0, and consequently $\dot{R}_{ice}$ decreases more drastically with concentration c_0 (5.5), compared with v_{ice} (figure 8*b*).

The growth rate of the ice particles $\dot{R}_{ice}$ is also non-dimensioned by the typical velocity of solute diffusion $v_{diff} = \mathscr{D}/D_0$. Then, the dimensionless growth rate of ice particles $\dot{R}_{ice}/v_{diff}$ can be described by the solutal Marangoni number Ma and the Stefan number St:

$$\frac{\dot{R}_{ice}}{v_{diff}} = \frac{v_{ice} D_0}{\mathscr{D}} \frac{c_p \Delta T}{L_f} \sim MaSt, \tag{5.6}$$

where $St = c_p \Delta T / L_f$ is the Stefan number (Zeng *et al.* 2022). This scaling relation (5.6) again agrees well with the experimental data, as shown in figure 9(*c*). Moreover, in the present experiments, evaporative cooling of the ethanol–water mixture has little effect on the reported interfacial freezing dynamics (see detailed analysis in Appendix B). By contrast, when a highly volatile liquid (e.g. ether) is mixed with another whose melting point is near room temperature (e.g. hexadecane), selective evaporation can release enough latent heat to freeze the droplet, as demonstrated by Kant *et al.* (2020*b*) and Zeng *et al.* (2023).

5.3. *Final wrapping state of the binary droplet*

Based on our understanding of ice particle dynamics, we now focus on the final wrapping state of freezing supercooled ethanol–water droplets, when the droplet is fully covered by dispersed ice particles, as shown in figure 10(*a–d*). With increasing concentration c_0, the final radius R_{final} of the ice particles is found to decrease, while the thickness h_{ice} of the ice particles increases, which can be inferred from the transparency of ice particles. The dependence of final wrapping state on concentration c_0 can be explained by considering the characteristic time scale τ_c for ice particles travelling across the droplet, $\tau_c \sim R_0/v_{ice}$, where $R_0 \approx 1$ cm is the initial radius of the droplet in experiments for all c_0. Then, the equivalent radius of ice particles R_{final} at the final wrapping state can be expressed as follows:

$$R_{final} = \tau_c \dot{R}_{ice} \sim \frac{c_p \Delta T R_0}{L_f}. \tag{5.7}$$

The predictions of the final radius of ice particles R_{final} well describe the trend of the experimental data, as shown in figure 10(*e*). From (5.7), the final radius of the ice particles R_{final} is found to be determined solely by the supercooling temperature ΔT. Therefore, the freezing point depression effect of the ethanol concentration c_0 results in the final radius of the ice particles R_{final} decreasing with concentration c_0. Then, the final radius R_{final} is further non-dimensioned by the radius of the droplet R_0, and the dimensionless radius of ice particles at the final state R_{final}/R_0 can be expressed as follows:

$$\frac{R_{final}}{R_0} = \frac{\tau_c \dot{R}_{ice}}{R_0} \sim St. \tag{5.8}$$

This scaling relation (5.8) is further validated by the experimental data, as shown in figure 10(*f*). Besides, as the concentration c_0 decreases, the characteristic time scale $\tau_c = R_0/v_{ice}$ also decreases. If we assume that the ice growth along the thickness direction

https://doi.org/10.1017/jfm.2025.11006 Published online by Cambridge University Press

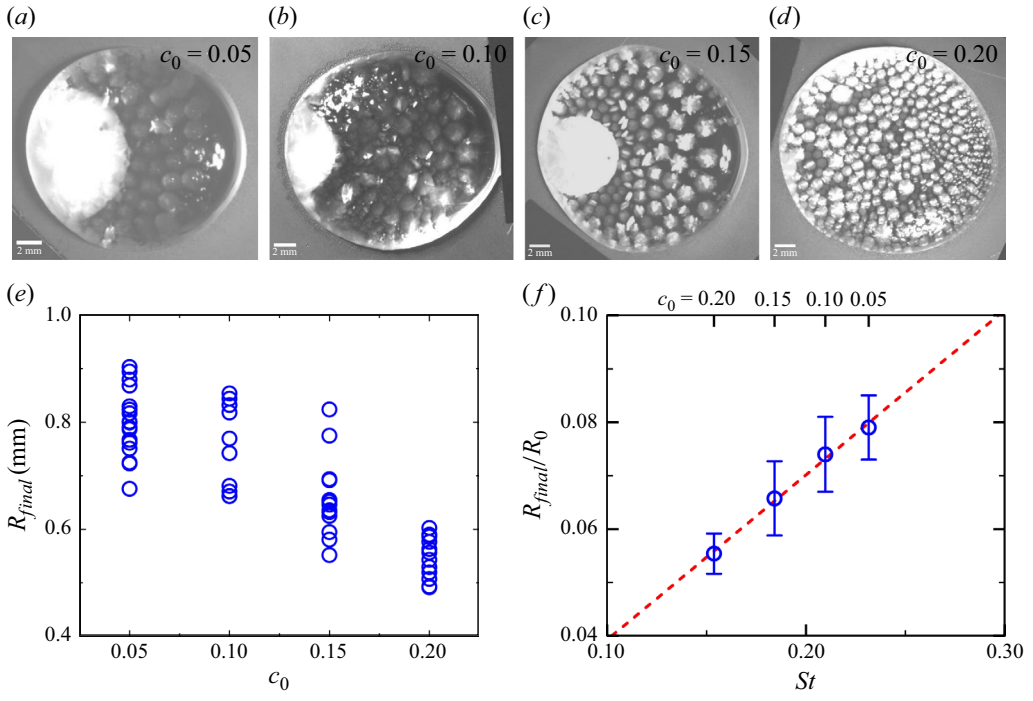


Figure 10. Final wrapping state of the frozen supercooled ethanol–water droplet. (*a–d*) Top-down view for the final wrapping state of the frozen supercooled ethanol–water droplets at different ethanol concentrations c_0. (*e*) Equivalent radius of ice particles R_{final} at the final wrapping state as a function of ethanol concentration c_0. (*f*) Dimensionless radius of ice particles R_{final}/R_0 at the final wrapping state as a function of Stefan number St. The dots are for the experimental data, the red solid lines are for the model predictions, and the red dashed line is for the linear relation between R_{final}/R_0 and St. The error bars are for the standard deviation of at least 15 data points.

obeys the diffusive growth dynamics $h_{ice} \sim \sqrt{\tau_c}$ (Ghabache, Josserand & Séon 2016), then the ice particles would be thinner and consequently more transparent as the concentration c_0 decreases.

6. Conclusion and discussions

In conclusion, we present a compelling study on the interfacial freezing dynamics of supercooled ethanol–water droplets, revealing the critical role of the internal solutal Marangoni flow, triggered by the localised enriched concentration of ethanol near the ice front. By incorporating the fluid's property variations, our model quantitatively predicts the ice particle's migration velocity via the Marangoni flow and its growth rate via a balance of latent heat and solutal-Marangoni-enhanced thermal dissipation.

Our findings may advance the fundamental understanding of complex physicochemical hydrodynamics in the context of multicomponent liquids undergoing phase transitions and may further pave the way for droplet-based technological innovations in manufacturing and material science (Lohse & Zhang 2020; Gao *et al.* 2025; Wang *et al.* 2025). More efforts are needed to understand the morphological evolution and instability of the solidification front within multicomponent liquid systems, spanning from the molecular scale (Facq, Danede & Chazallon 2013; Wahl *et al.* 2020) to the nanometre scale (Ahmadi *et al.* 2019; Grivet *et al.* 2022) and further to the macroscopic scale (Anderson & Guba

https://doi.org/10.1017/jfm.2025.11006 Published online by Cambridge University Press

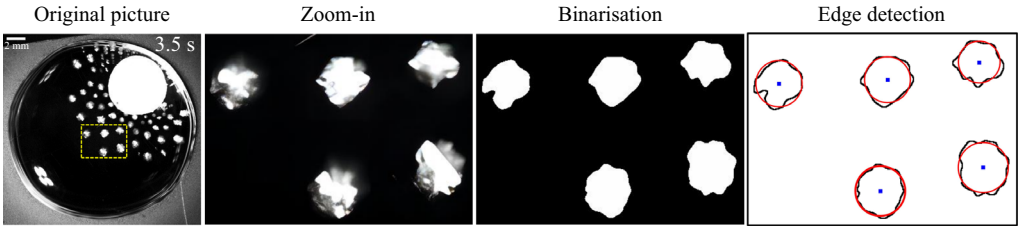


Figure 11. Image-processing procedure for analysing the displacement ξ and the radius R_{ice} of the ice particles. For a typical snapshot ($t = 3.5$ s in figure 4*c*), the original picture first undergoes binarisation and denoising. Then, using edge-detection methods, the outline of the ice particle is obtained. Subsequently, we can calculate the area S and the mass centre of the ice particle (x, y). Then, we calculate the equivalent radius $R_{ice} = \sqrt{S/\pi}$, under the assumption of the circular shape of the ice particle. We can also calculate the displacement $\xi = \sqrt{(x - x_0)^2 + (y - y_0)^2}$ of the ice particle, where (x_0, y_0) is the initial position of the ice particle.

2020; Du *et al.* 2025), especially when the solidification process is coupled with other physical processes, such as flash evaporation (Kant *et al.* 2020*b*; Zeng *et al.* 2023).

Supplementary movies. Supplementary movies are available at https://doi.org/10.1017/jfm.2025.11006.

Acknowledgements. We thank the anonymous reviewers for their insightful comments, which have greatly helped improve the clarity of this work.

Funding. This work is supported by NSFC Excellence Research Group Program for 'Multiscale Problems in Nonlinear Mechanics' (no. 12588201), the Natural Science Foundation of China under grant no. 12402321, the National Key R&D Program of China under grant no. 2021YFA0716201, the New Cornerstone Science Foundation through the New Cornerstone Investigator Program and the XPLORER PRIZE, the Postdoctoral Fellowship Program of the China Postdoctoral Science Foundation under grant nos 2025T180524, GZB20240366 and 2024M751637 and the Shuimu Tsinghua Scholar Program under grant no. 2023SM038.

Declaration of interests. The authors report no conflict of interest.

Appendix A. Imaging processing procedure

For a typical snapshot ($t = 3.5$ s in figure 4*c*), the original picture (the yellow dashed box) first undergoes binarisation and denoising, as shown in figure 11. The white region represents the ice particle. Then, we use edge-detection methods to obtain the outline of the ice particle, as indicated by the black solid line in the last image of figure 11. Subsequently, we can calculate the area S and the mass centre of the ice particle (x, y), as indicated by the blue dots in the last image of figure 11. Then, we calculate the equivalent radius $R_{ice} = \sqrt{S/\pi}$, under the assumption of the circular shape of the ice particle, as indicated by the red circles. Additionally, we can also calculate the displacement $\xi = \sqrt{(x - x_0)^2 + (y - y_0)^2}$ of the ice particle, where (x_0, y_0) is the initial position of the ice particle. Using these image-processing and data-processing procedures, the migration and growth dynamics of a single ice particle can be extracted from the experimental snapshots, as sketched in figure 7(*a*).

Appendix B. Discussions of the evaporation-cooling effect

To assess the influence of droplet evaporation on the observed interfacial freezing dynamics, we compute the evaporation rate of ethanol–water films (initial volume $V_0 = 500\ \mu$l, radius $R_0 = 1$ cm) with different ethanol fractions using the numerical models reported by Zeng *et al.* (2023) and Wakata *et al.* (2024, 2025). Figure 12 shows the ethanol evaporation rate for films with various ethanol fractions ($c_0 = 0.05, 0.10, 0.15, 0.20$).

https://doi.org/10.1017/jfm.2025.11006 Published online by Cambridge University Press

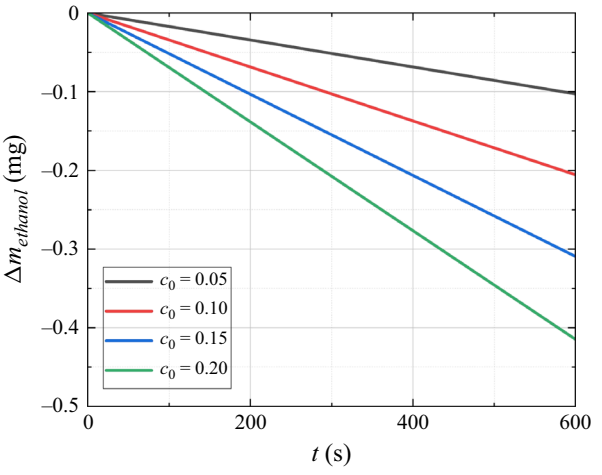


Figure 12. Ethanol evaporation rate of ethanol–water liquid films (initial volume $V_0 = 150\,\mu$l, radius $R_0 = 1$ cm) with various ethanol fractions.

The typical ethanol evaporation flux can be estimated as $\dot{m}_{ethanol} \sim 0.4\,\text{mg}/600\,\text{s} \sim 10^{-9}\,\text{kg s}^{-1}$. Therefore, the heat flux induced by ethanol evaporation can be estimated as follows:

$$Q_{evap} = L_e \dot{m}_{ethanol} \sim 10^{-6}\,\text{kJ s}^{-1}, \tag{6.1}$$

where $L_e = 841\,\text{kJ kg}^{-1}$ is the latent heat of vaporisation of ethanol.

By contrast, the typical growth rate of the ice particles $\dot{R}_{ice} \sim 1\,\text{mm s}^{-1}$, so the released latent heat of ice particle growth can be estimated as follows:

$$Q_{ice} = L_f \rho_{ice} \pi R_0 \dot{R}_{ice} \sim 10^{-1}\,\text{kJ s}^{-1}, \tag{6.2}$$

where $\rho_{ice} = 917\,\text{kg m}^{-3}$ is the density of ice.

The released latent heat of ice particle growth is much larger than the heat flux induced by ethanol evaporation, $Q_{ice} \gg Q_{evap}$. Therefore, ethanol evaporation has a negligible effect on the reported interfacial freezing dynamics.

References

Ahmadi, S., Nath, S., Kingett, C., Yue, P. & Boreyko, J. 2019 How soap bubbles freeze. *Nat. Commun.* **10** (1), 2531.

Anderson, D., Worster, M. & Davis, S. 1996 The case for a dynamic contact angle in containerless solidification. *J. Cryst. Growth* **163** (3), 329–338.

Anderson, D.M. & Guba, P. 2020 Convective phenomena in mushy layers. *Annu. Rev. Fluid Mech.* **52** (1), 93–119.

Boulogne, F. & Salonen, A. 2020 Drop freezing: fine detection of contaminants by measuring the tip angle. *Appl. Phys. Lett.* **116** (10).

Cebeci, T. & Kafyeke, F. 2003 Aircraft icing. *Annu. Rev. Fluid Mech.* **35** (1), 11–21.

Chu, F., Li, S., Zhao, C., Feng, Y., Lin, Y., Wu, X., Yan, X. & Miljkovic, N. 2024 Interfacial ice sprouting during salty water droplet freezing. *Nat. Commun.* **15** (1), 2249.

Dean, J.A. 1999 *Lange's Handbook of Chemistry*. McGraw Hill, Inc.

Dedovets, D., Monteux, C. & Deville, S. 2018 Five-dimensional imaging of freezing emulsions with solute effects. *Science* **360** (6386), 303–306.

Dehghani-Sanij, A., Dehghani, S., Naterer, G. & Muzychka, Y. 2017 Sea spray icing phenomena on marine vessels and offshore structures: review and formulation. *Ocean Engng.* **132**, 25–39.

Diddens, C. 2017 Detailed finite element method modeling of evaporating multi-component droplets. *J. Comput. Phys.* **340**, 670–687.

https://doi.org/10.1017/jfm.2025.11006 Published online by Cambridge University Press

DU, Y., WANG, F., CALZAVARINI, E. & SUN, C. 2025 Sea ice aging by diffusion-driven desalination. *Phys. Rev. Lett.* **135** (10), 104201.
DU, Y., WANG, Z., JIANG, L., CALZAVARINI, E. & SUN, C. 2023 Sea water freezing modes in a natural convection system. *J. Fluid Mech.* **960**, A35.
FACQ, S., DANEDE, F. & CHAZALLON, B. 2013 Ice particle crystallization in the presence of ethanol: an in situ study by raman and X-ray diffraction. *J. Phys. Chem. A* **117** (23), 4916–4927.
GAO, Y., CHEN, C., WANG, F., LI, M. & SUN, C. 2025 Characterization and removal of contaminants in lithography. *Sci. China Phys. Mech. Astron.* **68** (9), 294702.
GELDERBLOM, H., DIDDENS, C. & MARIN, A. 2022 Evaporation-driven liquid flow in sessile droplets. *Soft Matt.* **18** (45), 8535–8553.
GHABACHE, E., JOSSERAND, C. & SÉON, T. 2016 Frozen impacted drop: from fragmentation to hierarchical crack patterns. *Phys. Rev. Lett.* **117** (7), 074501.
GRAEBER, G., SCHUTZIUS, T., EGHLIDI, H. & POULIKAKOS, D. 2017 Spontaneous self-dislodging of freezing water droplets and the role of wettability. *Proc. Natl Acad. Sci.* **114** (42), 11040–11045.
GRIVET, R., MONIER, A., HUERRE, A., JOSSERAND, C. & SÉON, T. 2022 Contact line catch up by growing ice crystals. *Phys. Rev. Lett.* **128** (25), 254501.
GURGANUS, C., KOSTINSKI, A.B. & SHAW, R.A. 2013 High-speed imaging of freezing drops: still no preference for the contact line. *J. Phys. Chem. C* **117** (12), 6195–6200.
HALFPAP, B.L. & SORENSEN, C.M. 1982 The viscosity of supercooled aqueous solutions of ethanol and hydrazine. *J. Chem. Phys.* **77** (1), 466–471.
HU, M., WANG, F., TAO, Q., CHEN, L., RUBINSTEIN, S. & DENG, D. 2020 Frozen patterns of impacted droplets: from conical tips to toroidal shapes. *Phys. Rev. Fluids* **5** (8), 081601.
HUERRE, A., MONIER, A., SÉON, T. & JOSSERAND, C. 2021 Solidification of a rivulet: shape and temperature fields. *J. Fluid Mech.* **914**, A32.
JIANG, Y., ZHAO, Y., ZHANG, H., YANG, C. & CHENG, P. 2024 Three-dimensional shaping strategy via solidifying polygonal nanofluid drops. *Cell Rep. Phys. Sci.* **5** (4), 101904.
KANT, P., KOLDEWEIJ, R., HARTH, K., VAN LIMBEEK, M. & LOHSE, D. 2020*a* F*a*st-freezing kinetics inside a droplet impacting on a cold surface. *Proc. Natl Acad. Sci.* **117** (6), 2788–2794.
KANT, P., MÜLLER-GROELING, H. & LOHSE, D. 2020*b* Pattern formation during the impact of a partially frozen *b*inary droplet on a cold surface. *Phys. Rev. Lett.* **125** (18), 184501.
KAVURI, S., KARAPETSAS, G., SHARMA, C.S. & SAHU, K.C. 2023 Freezing of sessile droplet and frost halo formation. *Phys. Rev. Fluids* **8** (12), 124003.
KAVURI, S., KARAPETSAS, G., SHARMA, C.S. & SAHU, K.C. 2025 Evaporation-driven coalescence of two droplets undergoing freezing. *J. Fluid Mech.* **1006**, A21.
KHARAL, S. & LOUF, J. 2023 Unidirectional freezing of polymer solution droplets. *Langmuir* **40** (1), 118–124.
KHATTAB, I.S., BANDARKAR, F., FAKHREE, M.A.A. & JOUYBAN, A. 2012 Density, viscosity, and surface tension of water+ ethanol mixtures from 293 to 323k. *Korean J. Chem. Engng* **29**, 812–817.
KOLDEWEIJ, R., KANT, P., HARTH, K., DE RUITER, R., GELDERBLOM, H., SNOEIJER, J., LOHSE, D. & VAN LIMBEEK, M. 2021 Initial solidification dynamics of spreading droplets. *Phys. Rev. Fluids* **6** (12), L121601.
KUCHUK, V.I., SHIROKOVA, I.Y. & GOLIKOVA, E.V. 2012 Physicochemical properties of water-alcohol mixtures of a homological series of lower aliphatic alcohols. *Glass Phys. Chem.* **38**, 460–465.
LAMBLEY, H., GRAEBER, G., VOGT, R., GAUGLER, L., BAUMANN, E., SCHUTZIUS, T. & POULIKAKOS, D. 2023 Freezing-induced wetting transitions on superhydrophobic surfaces. *Nat. Phys.* **19** (5), 649–655.
LOHSE, D. & ZHANG, X. 2020 Physicochemical hydrodynamics of droplets out of equilibrium. *Nat. Rev. Phys.* **2** (8), 426–443.
LOLLA, V., AHMADI, S., PARK, H., FUGARO, A. & BOREYKO, J. 2022 Arrested dynamics of droplet spreading on ice. *Phys. Rev. Lett.* **129** (7), 074502.
LYU, S., ZHU, X., LEGENDRE, D. & SUN, C. 2023 Liquid encapsulation in a freezing sessile drop. *Droplet* **2** (4), e90.
MAKKONEN, L., LAAKSO, T., MARJANIEMI, M. & FINSTAD, K. 2001 Modelling and prevention of ice accretion on wind turbines. *Wind Engng* **25** (1), 3–21.
MARIN, A., ENRIQUEZ, O., BRUNET, P., COLINET, P. & SNOEIJER, J. 2014 Universality of tip singularity formation in freezing water drops. *Phys. Rev. Lett.* **113** (5), 054301.
MARIN, A., KARPITSCHKA, S., NOGUERA-MARÍN, D., CABRERIZO-VÍLCHEZ, M.A., ROSSI, M., KÄHLER, C.J., VALVERDE, R. & MIGUEL, A. 2019 Solutal marangoni flow as the cause of ring stains from drying salty colloidal drops. *Phys. Rev. Fluids* **4** (4), 041601.
MARIN, A., LIEPELT, R., ROSSI, M. & KÄHLER, C.J. 2016 Surfactant-driven flow transitions in evaporating droplets. *Soft Matt.* **12** (5), 1593–1600.

https://doi.org/10.1017/jfm.2025.11006 Published online by Cambridge University Press

DE RUITER, J., SOTO, D. & VARANASI, K. 2018 Self-peeling of impacting droplets. *Nat. Phys.* **14** (1), 35–39.
SCHNEIDER, C.A., RASBAND, W.S. & ELICEIRI, K.W. 2012 Nih image to imagej: 25 years of image analysis. *Nat. Methods* **9** (7), 671–675.
SCHREMB, M., CAMPBELL, J., CHRISTENSON, H. & TROPEA, C. 2017 Ice layer spreading along a solid substrate during solidification of supercooled water: experiments and modeling. *Langmuir* **33** (19), 4870–4877.
SEBILLEAU, J., ABLONET, E., TORDJEMAN, P. & LEGENDRE, D. 2021 Air humidity effects on water-drop icing. *Phys. Rev. E* **104** (3), L032802.
TEMBELY, M. & DOLATABADI, A. 2019 A comprehensive model for predicting droplet freezing features on a cold substrate. *J. Fluid Mech.* **859**, 566–585.
THIÉVENAZ, V., JOSSERAND, C. & SÉON, T. 2020 Retraction and freezing of a water film on ice. *Phys. Rev. Fluids* **5** (4), 041601.
THIÉVENAZ, V., SÉON, T. & JOSSERAND, C. 2019 Solidification dynamics of an impacted drop. *J. Fluid Mech.* **874**, 756–773.
WAHL, M.S., AASEN, A., HJELME, D.R. & WILHELMSEN, Ø. 2020 Ice formation and growth in supercooled water–alcohol mixtures: theory and experiments with dual fiber sensors. *Fluid Phase Equilibr.* **522**, 112741.
WAKATA, Y., CHAO, X., SUN, C. & DIDDENS, C. 2024 Evaporation of acoustically levitated bicomponent droplets: mass and heat transfer characteristics. *J. Fluid Mech.* **984**, A17.
WAKATA, Y., WANG, F., SUN, C. & LOHSE, D. 2025 Thermal-solutal-induced bistability of evaporating multicomponent liquid thin films. *Proc. Natl Acad. Sci.* **122** (6), e2418487122.
WANG, F., CHEN, L., LI, Y., GU, X., HUO, P., HU, M. & DENG, D. 2023 Droplet impacting on a supercooled immiscible liquid pool. *Phys. Fluids* **35** (8), 081701.
WANG, F., CHEN, L., LI, Y., HUO, P., GU, X., HU, M. & DENG, D. 2024 Self-lifting droplet driven by the solidification-induced solutal marangoni flow. *Phys. Rev. Lett.* **132** (1), 014002.
WANG, F., ZENG, H., PERALTA, S., SEBILLEAU, J., SUN, C. & LEGENDRE, D. 2025 The physics of icing drops under complex conditions. *Acta Mech. Sinica* **41** (7), 1–17.
WEI, B.-L., ZHANG, J. & NI, M.-J. 2025 A hybrid phase field-volume of fluid method for the simulation of three-dimensional binary solidification in the presence of gas bubble. *J. Comput. Phys.* **524**, 113720.
ZADRAŽIL, A., STEPANEK, F. & MATAR, O.K. 2006 Droplet spreading, imbibition and solidification on porous media. *J. Fluid Mech.* **562**, 1–33.
ZENG, H., LYU, S., LEGENDRE, D. & SUN, C. 2022 Influence of gravity on the freezing dynamics of drops on a solid surface. *Phys. Rev. Fluids* **7** (10), 103605.
ZENG, H., WAKATA, Y., CHAO, X., LI, M. & SUN, C. 2023 On evaporation dynamics of an acoustically levitated multicomponent droplet: evaporation-triggered phase transition and freezing. *J. Colloid Interf. Sci.* **648**, 736–744.
ZENG, H., WANG, F. & SUN, C. 2024 Extended spreading of saline droplets upon impact on a frosty surface. *Phys. Rev. Fluids* **9** (4), 044001.

https://doi.org/10.1017/jfm.2025.11006 Published online by Cambridge University Press